

Journal of Geophysical Research: Oceans

RESEARCH ARTICLE

10.1002/2017JC013568

Key Points:

- Measurements of differential pressure and wave parameters can be used to estimate wave-driven benthic exchange in the field
- Wave-induced benthic exchange rates exceeded current and tide-induced rates by over an order of magnitude in a shallow estuary
- Numerical model shows hydraulic diffusivity and wave parameters control wave-induced benthic exchange rate, depth, and residence time

Supporting Information:

- Supporting Information S1

Correspondence to:

H. A. Michael,
hmichael@udel.edu

Citation:

Russoniello, C. J., Heiss, J. W., & Michael, H. A. (2018). Variability in benthic exchange rate, depth, and residence time beneath a shallow coastal estuary. *Journal of Geophysical Research: Oceans*, 123, 1860–1876.
<https://doi.org/10.1002/2017JC013568>

Received 21 OCT 2017

Accepted 2 FEB 2018

Accepted article online 11 FEB 2018

Published online 8 MAR 2018

Variability in Benthic Exchange Rate, Depth, and Residence Time Beneath a Shallow Coastal Estuary

Christopher J. Russoniello^{1,2} , James W. Heiss^{1,3} , and Holly A. Michael^{1,4} 

¹Department of Geological Sciences, University of Delaware, Newark, DE, USA, ²Now at Department of Earth Sciences, Syracuse University, Syracuse, NY, USA, ³Now at The National Academy of Sciences, Washington, DC, USA, ⁴Department of Civil and Environmental Engineering, University of Delaware, Newark, DE, USA

Abstract Hydrodynamically driven benthic exchange of water between the water column and shallow seabed aquifer is a significant and dynamic component of coastal and estuarine fluid budgets. Associated exchange of solutes promotes ecologically important chemical reactions, so quantifying benthic exchange rates, depths, and residence times constrains coastal chemical cycling estimates. We present the first combined field, numerical, and analytical modeling investigation of wave-induced exchange. Temporal variability of exchange was calculated with data collected by instruments deployed in a shallow estuary for 11 days. Differential pressure sensors recorded pressure gradients across the seabed, and up- and down-looking ADCPs recorded currents and pressures to determine wave parameters, surface-water currents, and water depth. Wave-induced exchange was calculated (1) directly from differential pressure measurements, and indirectly with an analytical model based on wave parameters from (2) ADCP and (3) wind data. Wave-induced exchange from pressure measurements and ADCP-measured wave parameters matched well, but both exceeded wind-based values. Exchange induced by tidal pumping and current-bed form interaction—the other primary drivers in shallow coastal waters were calculated from tidal stage variation and ADCP-measured currents. Exchange from waves (mean = 20.0 cm/d; range = 1.75–92.3 cm/d) greatly exceeded exchange due to tides (mean = 3.7 cm/d) and current-bed form interaction (mean = 6.5×10^{-2} cm/d). Groundwater flow models showed aquifer properties affect wave-driven benthic exchange: residence time and depth increased and exchange rates decreased with increasing hydraulic diffusivity (ratio of aquifer permeability to compressibility). This new understanding of benthic exchange will help managers assess its control over chemical fluxes to marine systems.

1. Introduction

Estuaries and coastal seas are ecologically important systems that host diverse biological assemblages and reactive mixing zones driven by land-sea chemical gradients. Seabed sediments host high rates of chemical reactivity, and hydrodynamic mixing of water and solutes between seabed sediments and the overlying water column is an essential control on solute fluxes and reaction rates in these coastal ecosystems. In this work, we describe such mixing as *benthic exchange*, as defined in Boano et al. (2014). The benthic zone reactivity resulting from such hydrodynamic exchange has important effects on carbon and nitrogen cycling (e.g., Shum & Sundby, 1996). Benthic photosynthesis generates organic carbon at rates that equal or vastly exceed those of the overlying pelagic zone (e.g., Huettel et al., 2014; Nelson et al., 1999) by exploiting the high terrestrial-sourced nitrogen concentrations. On a larger scale, remineralization within sandy coastal sediments may account for 4–13% of total respiration on continental shelves (Huettel et al., 2014), and 44% of global denitrification is hosted within continental shelf sediments (Seitzinger et al., 2006). Clearly, understanding benthic exchange of fluid and solutes and quantifying the reaction rates accompanying such exchange is crucial for quantifying and managing nutrients and other chemicals in our coastal waters.

Solute reaction rates and removal efficiency are controlled by benthic exchange rate, exchange depth, and the residence time of water in these shallow seabed aquifers (e.g., Seitzinger et al., 2006). Benthic exchange rates control the flux of solutes to the benthic exchange zone (e.g., Sawyer, 2015). Benthic exchange depth, which defines reaction zone volume, is controlled by the length and time scales of the hydrodynamic forcing mechanism (e.g., Cardenas & Wilson, 2006; Jeng et al., 2001; Shum, 1993) as well as

the aquifer depth (e.g., Harrison et al., 1983; King et al., 2009) and hydraulic diffusivity (e.g., Ferris, 1952; Jeng et al., 2001; Mu et al., 1999), a ratio relating aquifer permeability to compressibility. Residence times, controlled by benthic exchange rates and depths, determine the time available for reactions to occur—removal efficiency is highest along shallow flow paths with short residence times when the residence time-scale matches the reactions timescale (Gomez-Velez et al., 2015; Harvey et al., 2013). These three controls all vary with spatial and temporal pressure variations induced by surface water hydrodynamics, which in turn depend on the seabed morphology and hydraulic properties of the shallow aquifer (e.g., Elliott & Brooks, 1997; Reid & Kajiura, 1957). Furthermore, exchange rates are especially high in dynamic estuarine and coastal waters because of shallow water depths and variable bathymetry, dynamic weather and tides, and a highly permeable seabed (e.g., Santos et al., 2012; Sawyer et al., 2013). Therefore, quantifying these three physical controls—benthic exchange rates, depths, and residence times—is crucial for understanding chemical cycling in coastal waters.

Currents (e.g., Ziebis et al., 1996), tides (e.g., Merritt, 2004), and waves (e.g., Thibodeaux & Boyle, 1987), have been identified as major hydrodynamic drivers of benthic exchange in shallow coastal waters. Tidally induced exchange is easily quantifiable because tides are predictable and easily measured, and the resulting exchange is unidirectional over measurement timescales and relatively uniform in space (e.g., Michael et al., 2003; Sawyer et al., 2013). Exchange induced by waves and currents is more difficult to quantify because they vary at small spatial and temporal scales that are difficult to measure, and because gross fluxes can be large, though net fluxes are zero (e.g., Riedl et al., 1972; Santos et al., 2012). Analytical and numerical models are excellent tools with which to estimate rates of exchange, especially over large areas (e.g., King, 2012; Riedl et al., 1972; Sawyer et al., 2013). However, these predictions require assumptions that may not always be reasonable, and depend on the available temporal and spatial resolution of field measurements of controlling parameters. These fluxes cannot be directly measured with traditional seepage meters because they cannot resolve the temporal and spatial scales associated with waves, seabed currents, and bed forms (e.g., Rosenberry, 2008; Russoniello & Michael, 2015; Smith et al., 2009), though automated seepage meters have resolved wave-induced flux variations at temporal resolutions as short as 15 s (Rosenberry & Morin, 2004). Heat can be used as a tracer to estimate fluxes and exchange depth, but it cannot be used to separate the components of exchange linked to different drivers (e.g., Wilson et al., 2016) and temperature-based methods lack the spatial (centimeters) and temporal (seconds) resolution to resolve exchange from individual waves (e.g., Briggs et al., 2012). Radioactive tracers such as Ra and Rn are unable to measure benthic exchange because the short residence times associated with the driving mechanisms are less than required to reach tracer equilibrium (e.g., Michael et al., 2011). Other methods, such as eddy correlation measurements (e.g., Berg et al., 2009; Crusius et al., 2008), can determine chemical fluxes near the seabed, but resolve fluxes on timescales much longer than those of benthic exchange. While fluxes may be determined from accurate measurements of the seabed pressure gradients or water column current velocities, such measurements require high temporal and spatial resolution, and the sensors must incur no large observer effect on the measured pressure gradients—a set of conditions which heretofore has been met only in laboratory conditions (e.g., Russoniello & Michael, 2015; Sawyer et al., 2011; Yamamoto et al., 1978).

Studies have used analytical models informed by environmental data to investigate the relative importance of different benthic exchange mechanisms at estuarine (e.g., Sawyer et al., 2013) and global (e.g., Santos et al., 2012) scales. However, these estimates have not been based on site-specific field data, as no study has measured the magnitude or temporal variability of wave-induced benthic exchange and its driving forces in the field at any scale. In this study, we calculated benthic exchange rates, depths, and residence times from high-resolution measurements of seabed pressure gradients and water column velocity profiles at a typical coastal site. We calculated absolute and relative exchange rates and examined temporal variability in benthic exchange induced by waves, tides, and currents. We also compared a number of different methods to calculate wave-induced benthic exchange in order to assess the accuracy of each in relation to the difficulty and cost of implementation. Finally, we investigated how the parameters most relevant for reactivity—wave-induced benthic exchange depths and residence times—vary with changing environmental conditions using numerical models. Ultimately these findings will inform geochemists and managers about benthic exchange and its effect on coastal chemical cycling and nutrient fluxes.

2. Background

2.1. Field Site

Indian River Bay, one of the Delaware Inland Bays, is a shallow (<3 m depth), microtidal (range ≈ 0.5 m) bay with an area of 37.9 km² (Figure 1). The Inland Bays host tourism and fisheries that are economically important to the State of Delaware (e.g., Latham & Lewis, 2012), but the bays have been subject to environmental declines linked to eutrophication due to development of nearby communities and historic and current agricultural activity (e.g., Walch et al., 2016). Previous studies have characterized the onshore and offshore hydrogeologic system at this site (e.g., Andres et al., 2017; Bratton et al., 2004; Russoniello et al., 2013; Sawyer et al., 2014).

2.2. Analytical and Empirical Equations for Calculation of Benthic Exchange Rates

Sawyer et al. (2013) identified waves, current/bed form interactions, and tides as the main physical drivers of benthic exchange in the Inland Bays (Figure 2). In this study, benthic exchange due to waves, current/bed form interactions, and tides are quantified using hydraulic gradients calculated from measured pore pressures and by applying measured hydrodynamic and environmental data to analytical and empirical equations. The equations used to calculate the exchange rates are given below.

Waves over a flat seabed drive surface water into the benthic zone beneath the wave peak (high head) out beneath the wave trough (low head) (Figure 2a). An analytical solution for wave-induced benthic exchange (q_w) across a flat seabed was developed by King et al. (2009):

$$q_w = \frac{Kh_w}{L_w \cosh \frac{2\pi d}{L_w}}, \quad (1)$$

where K is hydraulic conductivity, h_w is wave height, L_w is wavelength, and d is water depth. Wavelength was calculated using the dispersion equation:

$$\left(\frac{2\pi}{T_w}\right)^2 \approx g \frac{2\pi}{L_w} \tanh\left(\frac{2\pi}{L_w} d\right), \quad (2)$$

where T_w is wave period and g is gravity.

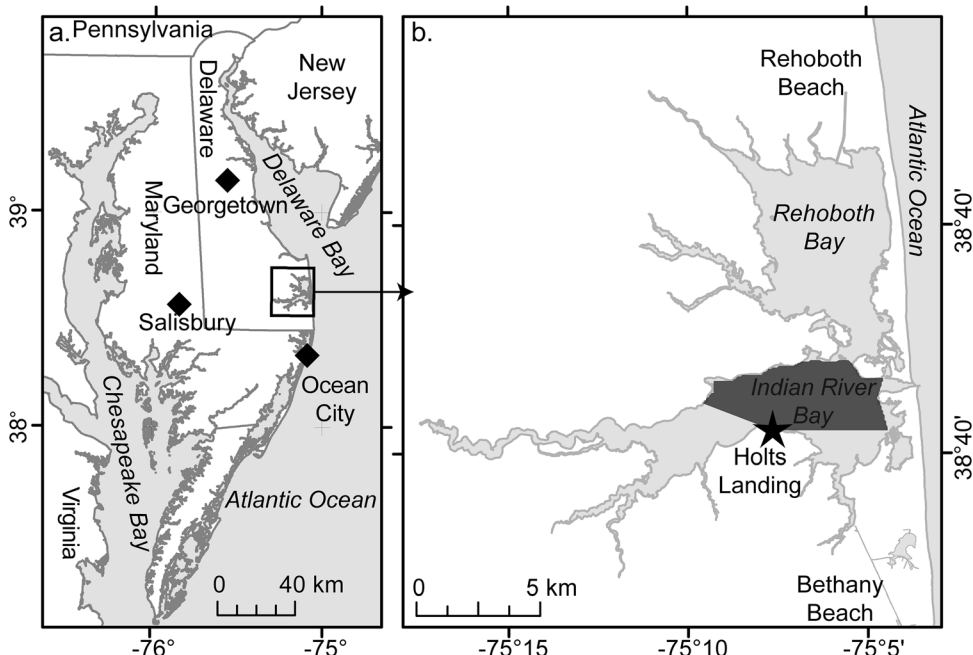


Figure 1. Site map. (a) State of Delaware, USA. Diamonds indicate three weather stations. (b) Holts Landing field site and vicinity. Star indicates tripod location. Dark shaded region indicates area from which wind fetch reaches tripod.

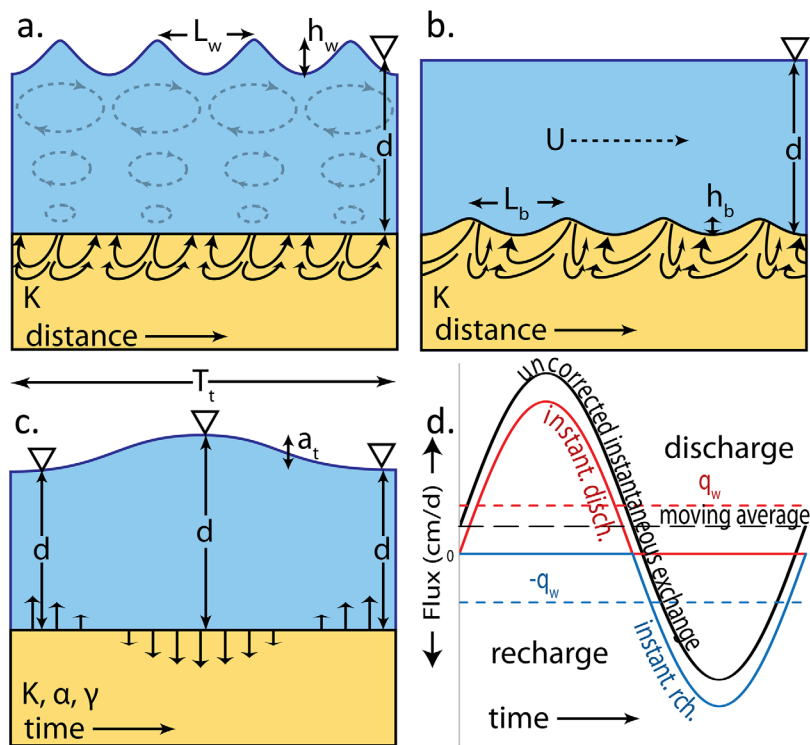


Figure 2. Schematic illustrating benthic flux drivers, groundwater flow paths, and parameters controlling each driver for (a) waves, (b) currents over bed forms, and (c) tidally induced benthic exchange. (d) Representation of terms used to describe different components of wave-induced benthic exchange. See section 3.1.3 for a description of these terms.

Wave period and wave height may be estimated from water depth, wind speed (W), and fetch (X) using empirical equations developed for a lake similar in fetch and depth to the Delaware Inland Bays (Young & Verhagen, 1996). This approach is similar to that of Sawyer et al. (2013) except that we use measured, rather than modeled, water depths.

$$T_w = \frac{7.52W}{g} \left[\tanh(0.331\delta^{1.01}) \tanh \left(\frac{0.0005215\chi^{0.73}}{\tanh(0.331\delta^{1.01})} \right) \right]^{0.37}, \quad (3)$$

$$h_w = \frac{0.241W^2}{g} \left[\tanh(0.493\delta^{0.75}) \tanh \left(\frac{0.00313\chi^{0.57}}{\tanh(0.493\delta^{0.75})} \right) \right]^{0.87}, \quad (4)$$

where χ is dimensionless fetch ($\chi = Xg/W^2$) and δ is dimensionless water depth ($\delta = dg/W^2$). We used local depth, corrected for tide, rather than fetch-averaged depth, as T_w and h_w were relatively insensitive to water depth over the fetch in this shallow estuary (Sawyer et al., 2013).

Currents over bed forms induce flux across the seabed due to the head difference between the up-current and leeward sides of individual bed forms (Figure 2b). The amplitude of head variation (a_b) due to current passing over periodic bed forms was described empirically by Fehlman (1985):

$$a_b = 0.28 \frac{U^2}{2g} \begin{cases} \left(\frac{h_b}{0.34d} \right)^{3/8} & h_b/d \leq 0.34 \\ \left(\frac{h_b}{0.34d} \right)^{3/2} & h_b/d \geq 0.34 \end{cases}, \quad (5)$$

where U is mean flow velocity in the water column, h_b is bed form height, and g is gravity. The benthic exchange induced by interactions between currents and bed forms (hereafter: *current-induced*) was described by Elliott and Brooks (1997):

$$q_b = \frac{2K a_b}{L_b}, \quad (6)$$

Tides induce benthic exchange because the compressible aquifer stores and releases water back to the water column as tides rise and fall (Figure 2c). Tide-induced benthic exchange was calculated as (Sawyer et al., 2013):

$$q_t = 2 \sin\left(\frac{\pi}{4}\right) \frac{a_t K(1-\gamma)}{\sqrt{\pi D T_t}}, \quad (7)$$

where T_t is the tidal period, a_t is the tidal amplitude, γ is the loading efficiency, and D is hydraulic diffusivity (K/S_s), where S_s is specific storage of the aquifer sediments. We assigned a γ of 0.9 as in Sawyer et al. (2013), which is a reasonable value for sediments (e.g., Wang, 2000; Younger, 1993) (supporting information Figure A1).

3. Methods

3.1. Field Instrumentation and Data Collection

3.1.1. Seabed Hydraulic Properties

A grain size analysis was performed on five seabed sediment samples collected near the tripod. Sediments were collected using a 5 cm × 20 cm bucket auger and were oven-dried at 80° overnight before being sorted with -1, 0, 1, 1.5, 1.75, 2, 2.5, 2.75, and 3 phi sieves. K values for each sample were determined with an Excel spreadsheet, HydroGeoSieveXL (Devlin, 2015), which calculates K from grain size with 15 different methods and informs the user whether the sediment statistics permit the use of each method for that sample. Hydraulic conductivity values calculated from grain size analysis for six sediment samples averaged 27.5 ± 4.0 m/d and ranged from 22.2 to 32.4 m/d (See supporting information Appendix A for full analysis results). These values are consistent with the observed medium-coarse nature of the seabed sand (e.g., Fetter, 2001). We assigned each sample a K value equal to the arithmetic mean K value (27.5 m/d) of all methods and applied the mean of these means as the K value for all calculations and models throughout this study.

3.1.2. Tripod

An instrument tripod was constructed and installed offshore of Holts Landing State Park in Indian River Bay, DE, USA to measure surface water wave and current parameters and pressure gradients across the seabed from which benthic exchanges could be calculated (Figure 3). The sensor tripod was deployed ~70 m from the coastline in water that averaged ~1 m depth (Figures 1 and 3). Three 3.8 cm diameter 6 m long steel pipes were vibrated 3 m into the seabed to form an equilateral triangular footprint with 2.5 m sides. These three pipes were connected by four 3 m horizontal pipes which stabilized the uprights and provided mounting points for sensors. The tripod and associated sensors were deployed and collected data between 16 and 27 October 2014.

3.1.3. Differential Pressure Measurements

Six Validyne P24 differential pressure sensors were deployed to measure pressure gradients across the seabed (Validyne, 2014). In these sensors, a difference in pressure between the two ports induces flexing in a metal diaphragm, which in turn produces a ± 5 V analog DC output with an error equivalent to 0.250% of full scale. We selected "dash 28" diaphragms with a 56 cm H₂O range, so that each sensor has an error of 1.4 mm H₂O. A length of polyethylene tubing (approximately 6 m × 1/16" inner diameter and 1/8" outer diameter) was attached to both the positive and negative orifices of each differential

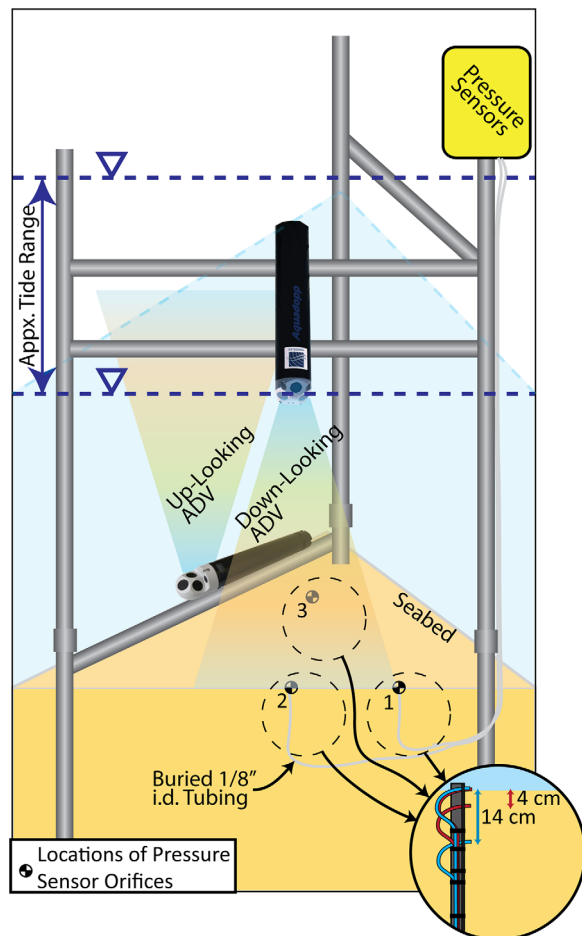


Figure 3. Field deployment schematic illustrating tripod components including frame, up and down-looking ADCPs, six differential pressure sensors within a pole-mounted waterproof case, associated tubing, and locations of tubing orifices. The orifices for two sensors—both a shallow (0–4 cm) and a deep (0–14 cm)—were located at locations 1, 2, and 3. Inset illustrates how tubing for both a shallow (red) and deep (blue) tube was installed and anchored using an aluminum rod at each of the three locations. Differential pressures were measured between tube ends in shallow (sensors 1s, 2s, and 3s) and deep (sensors 1d, 2d, and 3d) tubes. Note that data from only five sensors are presented because data from the deep sensor at location 3 (3s) was erroneous.

pressure sensor so that pressures were measured between the positive and negative tubing ends. Tubing and sensors were filled with degassed water (hot tap water further degassed by applying negative pressure with a syringe) to minimize compressibility between the orifice and diaphragm. The translucent tubing was examined immediately before deployment to confirm that no bubbles were present. Analog voltage signals from the differential pressure sensors were digitized and logged with a Campbell CR1000 logger at 10 Hz. The differential pressure sensors, logger, and two 12 v batteries were mounted in a waterproof case installed well above the high tide level on an upright pole of the tripod (Figure 3). Prior to deployment, each sensor was zeroed and a calibration curve between pressure and voltage was established for each sensor.

The six differential pressure sensors were deployed in three pairs of two to measure differential pressure between 0 and 4 cm depth and 0 and 14 cm depth at three locations. Hereafter, each differential pressure sensor is described first by the mounting rod to which the tubing was attached (1, 2, or 3) and then by the depth of the lower tube "s" (for shallow) or "d" (for deep), such that the six differential pressure sensors are described as 1s, 1d, 2s, 2d, 3s, and 3d. Prior to deployment, tubing ends were firmly attached to three 0.5 m long aluminum mounting rods (Figure 3 inset) and tubing orifices were wrapped in fine nylon screen material. The mounting rods were pushed vertically into the seabed, taking care not to damage the tubing, until the upper orifice of each tube was level with the seabed. The three mounting rods were spaced 1 m apart in a triangular pattern. The 12 tubes were routed through a trench to the base of the tripod and up the tripod leg to the waterproof case. A burst of data was recorded at 10 Hz for 6 min every hour, on the hour, resulting in 2,400 differential pressure measurements per sensor per hour—a total 4,680,000 differential pressure values over the 11 day deployment. Sensor 3s had a clear and large drift during the deployment and data from that sensor was discarded, thus we only present data from the remaining five sensors.

Voltage data were converted to differential pressure by applying the calibration. Hydraulic gradients calculated from this differential pressure were used with Darcy's law to calculate *uncorrected instantaneous exchange* (Figure 2d). A 60 s moving average was calculated and subtracted from uncorrected instantaneous exchange to calculate *instantaneous exchange*. By subtracting the moving average, pressure gradients that remain constant over time scales longer than 1 min are removed (possibly induced by tides, persistent currents, terrestrial gradients, or drift in the pressure sensor). The positive and negative values of instantaneous exchange are *instantaneous discharge* and *recharge*, respectively. The magnitudes of burst-averaged instantaneous discharge and recharge are equal, describe the same value (q_w) as equation (1), and are thus referred to as *wave-induced benthic exchange*. This value describes the one-way benthic exchange induced by waves into or out of the seabed.

3.1.4. ADCP Data

Two 2 MHz Aquadopp HR Acoustic Doppler Current Profilers (ADCP) were mounted to the tripod crossbars to measure velocity profiles, water depth as it varied with tide, and to calculate wave parameters (Nortek, 2010). The ADCPs internally logged three orthogonal velocity vectors (east, north, and up) and pressure for each depth interval or *bin* of each profile. All calculations using parameters measured by the ADCPs were based on this "east, north, up" data. The compass built into each ADCP was calibrated immediately prior to deployment. In order to prevent interference between the sonars, one ADCP recorded a "burst" of data every 60 min on the hour while the other ADCP recorded every 60 min on the half hour. Tide-induced benthic exchange values were calculated with tide elevation (from ADCP pressure data) and equation (7). A tidal amplitude was determined for each ebb and flood tide from which tide-induced exchange rates were calculated.

An *up-facing* ADCP was mounted to the instrument frame to measure velocity profiles in the water column, with the ADCP head 0.21 cm above the seabed. Twelve bins were spaced at 10 cm with a 20 cm blanking distance. Bursts of data were recorded at 4 Hz for 10 min every hour on the half-hour. The values recorded by this ADCP were linearly interpolated from the nearest value ahead of and behind the hour for direct comparison. The PUV method was used to estimate wave parameters (T_w and h_w) and wave direction from pressure (P) and the two horizontal velocity components (\vec{u} and \vec{v}) (Nortek, 2010). Pressure and the average velocities from cells 2 through 4 (depth range = 51–81 cm above seabed) were used for these calculations. The wave period for each burst was also calculated with two additional methods: (1) from a Fourier Transform of differential pressure sensor data for each burst, and (2) from the frequency of peaks in the smoothed ADCP pressure signal. The three methods matched well, and the PUV-derived T_w value was assigned in all except 41 of the 260 bursts, in which the PUV script could not assign a T_w value. In these 41 bursts, the average value from the peaks and differential pressure methods was assigned as the T_w value.

Wave-induced benthic exchange was calculated from these data and equations (1) and (2) for each burst and compared to benthic exchange calculated from differential pressure sensor data. Wave-induced benthic exchange calculated from ADCP-derived wave parameters is hereafter the *ADCP method*.

A second *down-facing ADCP* was mounted to the tripod to measure currents at the seabed. The head was 75 cm above the seabed and directly above pressure sensor 1s and 1d. The blanking distance was set to 10 cm and bin spacing was set to 2 cm for a total of 33 bins. Data were logged at 1 Hz in 5 min bursts every hour on the hour. The tide level dropped below the ADCP head during three low tides with corresponding gaps in data. Mean flow velocity (U) for each burst was calculated from the middle one-third of the down-looking ADCP velocity profile in order to remove noisy data at the profile top and bottom linked to low tide and bin-overlap with the seabed. Current-induced benthic exchange was calculated using equations (5) and (6) from these data and, because we did not measure bed form dimensions, across a reasonable range of L_b and h_b values ($L_b = 0.01\text{--}0.5\text{ m}$, $h_b = 0.01\text{--}0.1\text{ m}$).

3.2. Wind Data

Wave-induced benthic exchange was also calculated from wind velocity and direction data collected at the three nearest National Weather Service weather stations during October 2014 (NCDC, 2016). Georgetown, DE (GED, 929 records), Ocean City, MD (OXB, 976 records), and Salisbury, MD (SBY, 969 records) were 43.5, 23.0, and 31.6 km from the study site, respectively (Figure 1a). Wind fetch was measured in Google Earth as the distance between the tripod and the far shore for all compass directions (Figure 1b) and assigned based on measured wind direction (10 degree resolution). Wind velocity and direction data were processed with equations (2–4) to obtain wave parameters, which were used in equation (1) to obtain wave-induced benthic exchange values. These were compared to wave-induced benthic exchange calculated from differential pressure sensors and ADCP data. Wave-induced benthic exchange calculated from wind-derived wave parameters is hereafter the *wind method*. Wind records are recorded at irregular intervals (47 min average), so for comparison to other measurements collected on the hour, wind-based wave-induced benthic exchange rates were linearly interpolated from the nearest value ahead and behind the hour.

3.3. Numerical Groundwater Flow Modeling

Transient groundwater flow models were constructed using MODFLOW-2005 (Harbaugh et al., 2000) to investigate the effects of wave parameters, water depth, and aquifer parameters (S_s and K) on groundwater velocities, benthic exchange zone depth, and residence times in seabed aquifers under the influence of waves. A sensitivity analysis showed that wave-induced flux depends on hydraulic diffusivity ($D = K/S_s$) rather than K or S_s alone, so the field-measured K value was held constant in all model runs while S_s was varied.

A total of 2080 MODFLOW simulations were constructed and run to represent wave conditions of each of the 260 measured bursts and for each of eight values of S_s . Each set of 260 models was assigned a single S_s value from 10^{-2} to $10^{-5.5}\text{ m}^{-1}$ at half-magnitude intervals (supporting information Figure A1). Three model sets ($S_s = 10^{-2}$, 10^{-3} , and 10^{-4} m/s) are presented in greater detail herein than the other five sets.

Each 2-D cross-sectional MODFLOW model (100 layers by 120 columns) was assigned a thickness of L_w , which is twice the depth of $L_w/2$ expected for wave-induced benthic exchange (e.g., King et al., 2009) (Figure 4). Model columns were assigned a width of $L_w/40$ and each stress period (1 time step per stress period) was assigned a duration of $T_w/20$ (i.e., waves are each 40 cells wide and 20 stress periods long). Each model was run for $T_w \times 50$ s, or 1,000 stress periods. Results were calculated based on one wavelength in the middle of the domain (columns 41–80) to avoid potential edge affects along the model boundaries, and the last wave period (stress periods 981–1,000) to ensure that dynamic steady state had been achieved.

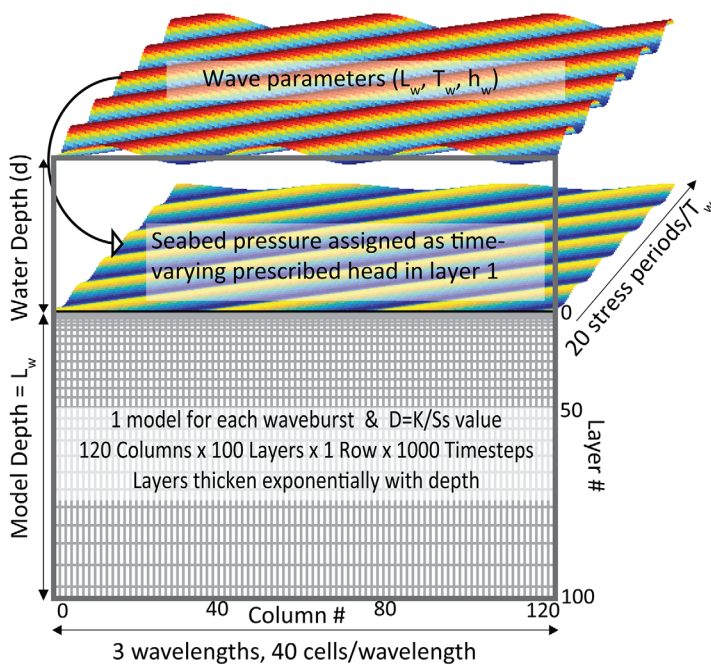


Figure 4. Modflow model schematic of geometry and boundaries.

For each stress period, a wave-induced hydraulic head was prescribed to all cells across the top model layer using the MODFLOW "Time-Variant Specified-Head" package (Harbaugh et al., 2000). The space and time-varying seabed pressure value was calculated with linear wave theory (e.g., King et al., 2009), which depends on T_w , h_w , and d . In each stress period, the wave pressure signal on the seabed migrated a distance $1/20 L_w$ (1 column). The pressure signal therefore repeated after one wave period. All other model boundaries were prescribed as zero flow.

For each model, a representative residence time (R_k) was calculated for each layer (k) as:

$$R_k = \sum_{n=1}^k \frac{V_k}{|Q_w|}, \quad (8)$$

where V_k is the volume of a cell in layer k , and $|Q_w|$ is the mean magnitude of the vertical component of wave-induced groundwater flow measured across the top boundary of cells in that layer. The R_k value may be considered a description, on average, of the age of water at a certain depth. This calculation makes several assumptions and it is not intended to be an exact value of residence time. However, R_k is a useful indicator to identify how wave and aquifer parameters affect the residence time of water in the benthic exchange zone.

4. Results

4.1. Wave-Induced Benthic Exchange

4.1.1. Field-Based Analysis

Wave-induced benthic exchange rates calculated from the five differential pressure measurements averaged 20.0 cm/d and ranged from 1.75 to 92.3 cm/d over the 260 bursts (Figures 5a, 5g, supporting information Figure A2, and Table 1). The average wave-induced benthic exchange from shallow sensor measurements was 29.1 cm/d, or 217% of the average wave-induced benthic exchange from deep sensor measurements. Thus, only about one-half of the wave-induced pressure amplitude was measured at 14 cm depth (deep sensors) compared to 4 cm depth (shallow sensors), indicating that wave-induced pressure gradients are attenuated rapidly with depth in the aquifer. Wave-induced instantaneous exchange had a maximum rate of 1,613 cm/d (0.19 mm/s; 5 sensor average) during the course of the study. In a given burst, the maximum instantaneous exchange measured with a differential pressure sensor wave-induced benthic exchange rate (q_w) by an average of about 1 order of magnitude (8.2–10.1 times for the five sensors).

Wave-induced benthic exchange calculated analytically (equation (1)) from ADCP-based wave parameters averaged 22.5 cm/d (Figures 5b, 5g, Table 1). Values of h_w calculated with the PUV method averaged 7.5 cm and T_w values averaged 1.62 s. Burst-averaged velocity magnitudes from the up-looking ADCP averaged 7.7 ± 3.0 cm/s and ranged from 1.6 to 14.0 cm/s.

Wave-induced benthic exchange calculated from wave conditions derived from wind data averaged 11.7 cm/d (Figure 5g, Table 1). During the experiment, winds were predominantly northerly and southerly. The resulting fetch was bimodally distributed (Figure 5c) because southern shorelines are close (148 m average), whereas northern shorelines are far (3.3 km average; Figure 1b). Wind velocities averaged 3.70 ± 2.40 m/s with sustained winds measured up to 13.4 m/s (Figure 5d). Wave parameters (h_w and T_w) calculated with the wind data from the three NOAA wind stations were similar (Figures 5e, 5f, Table 2). Wind-derived h_w and T_w values matched well with those calculated from ADCP data when fetch was long, but not as well when fetch was short (Figures 5c, 5e, and 5f). Wave-induced benthic exchange calculated with the wind method followed a similar trend as those calculated with the differential pressure and ADCP methods, but averaged about half (59% and 52%, respectively). This was largely due to the short fetches from southerly winds produced calculated wave conditions that were less energetic than those measured locally (Figures 5c, 5d, and 5g).

4.1.2. Groundwater Flow Model Results

Numerically simulated wave-induced benthic exchange from the set of high-D models matched well with the wave-induced benthic exchange calculated from the differential pressure measurements and ADCP methods (Figure 6a). This agreement is expected because a low compressibility assumption (reasonable for the sandy sediments) and identical wave conditions were prescribed for both the numerical and analytical solutions. Modeled wave-induced benthic exchange from the low-D models averaged 5.3 times greater

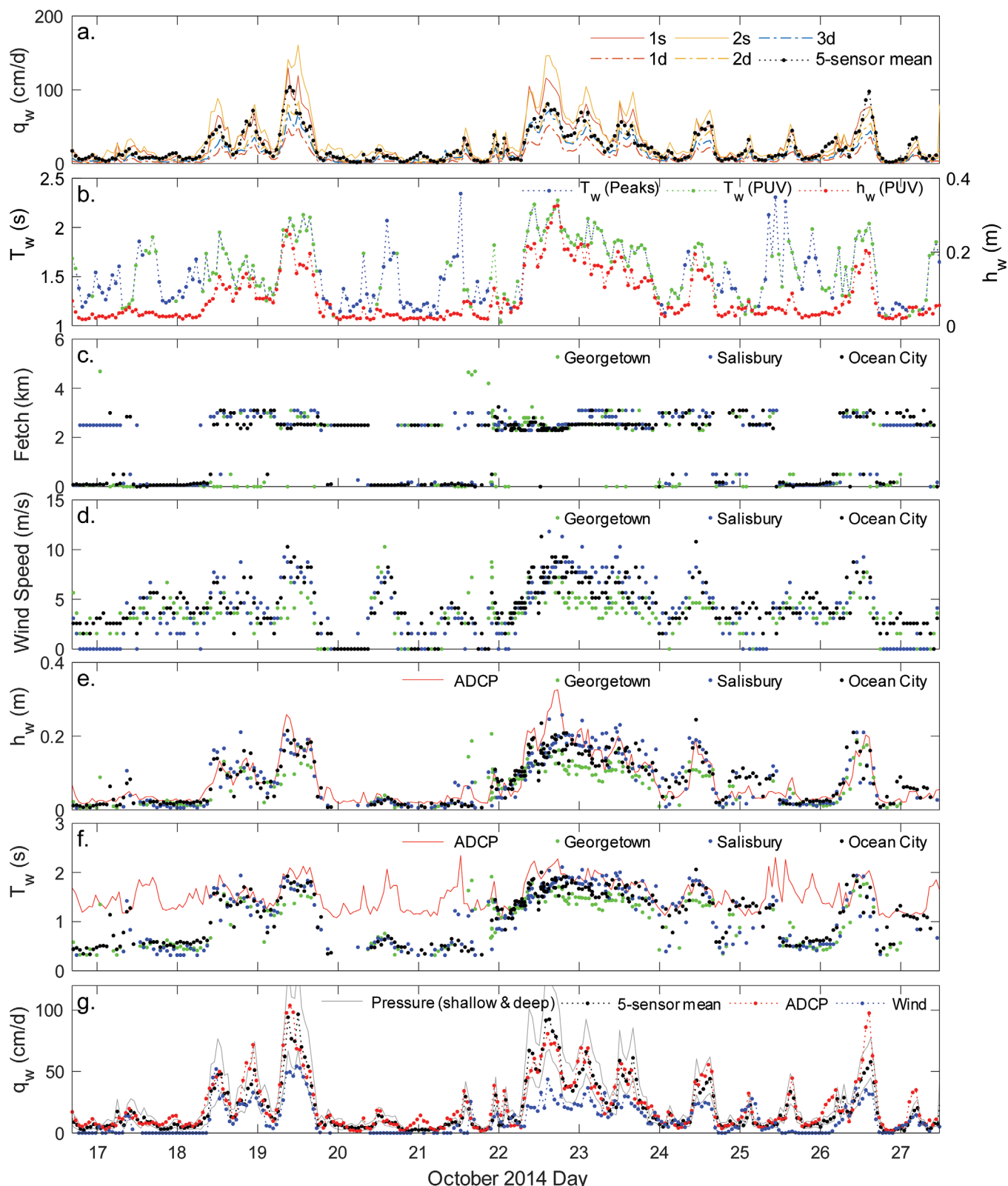


Figure 5. Hourly ADCP-and-wind-generated wave parameters and wave-induced benthic exchange values. (a) Individual and mean wave-induced benthic exchange rates calculated from data collected with five pressure sensors. Shaded green region below 10 cm/d represents the measurement error (see discussion in section 5.3). (b) ADCP-derived significant wave height (h_w) and peak period (T_w) from peaks and PUV methods. Wind (c) fetch and (d) velocity for data from three weather stations. (e) Significant wave height and (f) wave period from ADCP and wind data. (g) Wave-induced exchange rates calculated from pressure sensors (5 sensor average in black, the 2 sensor shallow average, and 3 sensor deep average bracket the gray region), and ADCP-derived and wind-derived wave parameters.

Table 1*Burst-Averaged Wave, Current, and Tide-Induced Benthic Exchange Rates*

	Wave-induced (q_w) (cm/d)									
	Differential pressure sensors			Groundwater models						
	Shallow sensors	Deep sensors	5 sensor mean	ADCP	Wind	$S_s = 10^{-2}$	$S_s = 10^{-3}$	$S_s = 10^{-4}$	Current-induced ^a (q_b) (cm/d)	Tide-induced (q_t) (cm/d)
Mean	1s: 25.78 2s: 32.47	1d: 9.49 2d: 17.38 3d: 14.64	19.96	22.47	11.71	105.80	34.74	16.58	0.07	3.43
Median	1s: 13.46 2s: 19.29	1d: 4.46 2d: 9.84 3d: 8.08	11.08	13.40	06.78	45.06	14.98	08.19	0.04	3.43
Min	1s: 1.76 2s: 2.92	1d: 0.77 2d: 0.98 3d: 0.79	1.75	01.47	0.00	01.57	0.69	0.62	0.00	2.34
Max	1s: 113.95 2s: 148.32	1d: 49.97 2d: 81.16 3d: 69.71	92.30	103.76	87.85	596.75	194.03	82.28	0.47	4.62
σ	1s: 26.45 2s: 31.38	1d: 10.66 2d: 17.57 3d: 15.09	20.05	21.42	13.11	129.59	42.10	18.01	0.08	0.50
CV ^b	1s: 1.03 2s: 0.97	1d: 1.12 2d: 1.01 3d: 1.03	1.00	0.95	1.12	1.22	1.21	1.09	1.20	0.15

Note. All values in table are mean value over the 260 bursts.

^aThe current-induced values assume the tallest, steepest bed form. ^bCoefficient of variation (CV) = σ/mean .

than the wave-induced benthic exchange calculated with the ADCP method (average = 105.8 cm/d; Figure 6a and Table 1), because the numerical model accounted for the highly compressible aquifer. Numerically simulated wave-induced benthic exchange followed the same trends as wave-induced benthic exchange calculated with the other three methods for all tested values of D.

Simulated exchange zone thicknesses were proportional to both L_w and D. For simplicity, the exchange zone is defined as the zone in which vertical wave-induced groundwater flow in the seabed aquifer exceeds 5% of the wave-induced benthic exchange across the seabed, the thickness of which is denoted d_{ex} .

In the set of high-D models representative of the relatively incompressible and permeable aquifer at the study site ($D = 3.18 \times 10^6$ m/s), d_{ex} averaged 1.69 m (Figure 6d). This d_{ex} value is 97% of $L_w/2$, which is the depth that surface waves are predicted to influence according to analytical solutions that neglect sediment

Table 2*Wave Parameters Calculated with Different Methods*

	Calculation method	Mean	σ	Min.	Max.
Wave Period (T_w)	PUV	1.62	0.29	1.04	2.28
	Peaks	1.60	0.33	1.08	2.34
	Differential pressure sensors	1.66	0.32	1.08	2.93
	Applied T_w value ^a	1.62	0.30	1.04	2.34
	Wind: Georgetown	0.69	0.57	0.00	1.97
	Wind: Ocean City	0.74	0.57	0.00	2.11
	Wind: Salisbury	0.85	0.56	0.00	2.06
	Wind: Average	0.54	0.57	0.00	2.11
	PUV	7.51	6.69	1.61	32.5
	Wind: Georgetown	4.37	4.95	0.00	21.1
Wave Height (H_w)	Wind: Ocean City	4.75	5.49	0.00	25.8
	Wind: Salisbury	5.60	5.37	0.00	24.5
	Wind: Average	4.91	5.27	0.00	25.8

^avalue used to calculate wave-induced benthic exchange from the ADCP method.

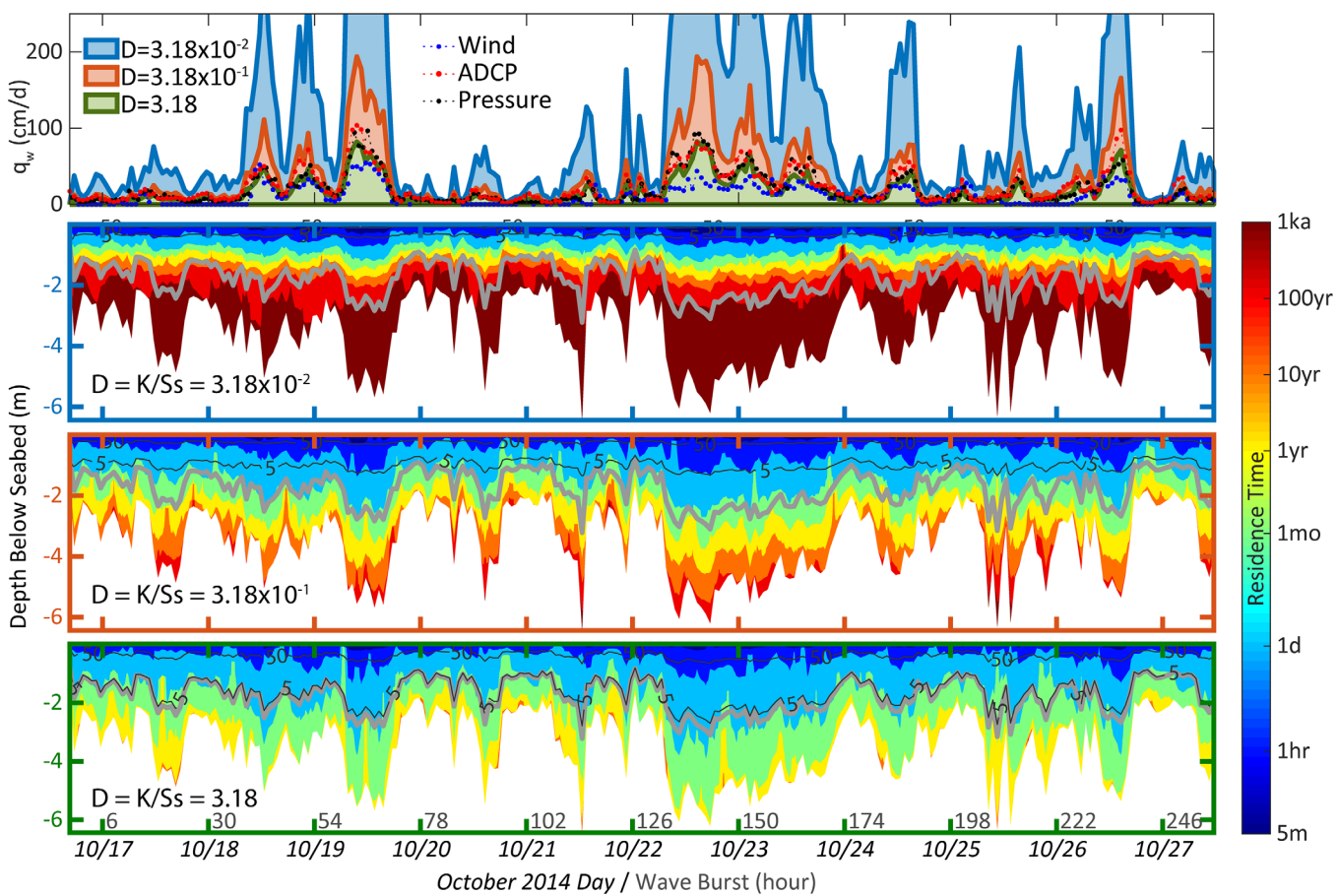


Figure 6. Effect of wave parameters and hydraulic diffusivity on q_w , residence time, and depth of wave-induced flux. (a) Comparison of wave-induced benthic exchange rates from numerical models and calculated from field data. Figures 6b, 6c, and 6d show average residence time (colorplots) and mean depth of flux (black contours) for each of 260 Modflow model runs. Model thickness was prescribed as L_w , which varied between wave bursts, so the model thickness and depth of plotted data vary temporally. Hydraulic diffusivity was assigned as 3.18×10^{-2} , 10^{-1} , and 10^0 to represent clay, sand, and gravel for models presented in Figures 6b, 6c, and 6d, respectively. The labeled black contours show depths at which vertical flux magnitudes are 50% and 5% of benthic exchange across the bed—the 5% contour (d_{ex}) approaches a depth of $L_w/2$ (gray contour) at high hydraulic diffusivity (Figure 6d).

compressibility (e.g., King et al., 2009). The benthic exchange zone thickness decreases markedly as D decreases: d_{ex} averages 1.01 m (58% of $L_w/2$) and 0.37 m (21% of $L_w/2$) for intermediate- D (3.18×10^{-1} m/s; Figure 6c), and low- D (3.18×10^{-2} m/s; Figure 6d) models, respectively. Because L_w varied during the course of the study, the exchange zone was also highly variable for all model sets. No correlation appears to exist between d_{ex} and either h_w or d .

Average residence times increased with depth for all model cases—the increase with depth was most rapid in the low- D model where the exchange zone was thinnest, whereas the rate of increase of residence time was lowest in the high- D model where the exchange zone was thickest (Figures 6b–6d). The thin, low- D exchange zone, combined with high exchange rates, results in a short mean residence time of just 5.5 days (Figure 6b). Residence times were longer in the higher- D model sets, with larger d_{ex} values—the residence time in the intermediate- D , and high- D aquifers average 70.9 and 183.3 days, respectively (Figures 6c and 6d). Residence time has a strong correlation with L_w ($r^2 = 0.98$, 0.99, and 0.97 in low- D , intermediate- D , and high- D model sets, respectively), but a correlation to h_w and d was not observed.

4.2. Current and Tide-Induced Benthic Exchange

Estimates of current-induced benthic exchange, calculated from down-looking ADCP-measured currents (Figures 7a and 7b), water depth (Figure 7b), and assumed bed form dimensions were consistently much less than wave and tide-induced benthic exchange during the measurement period (Figure 7c, Table 1). Near-bed currents measured with the down-looking ADCP averaged 3.0 ± 1.3 cm/s (red line in Figure 7b),

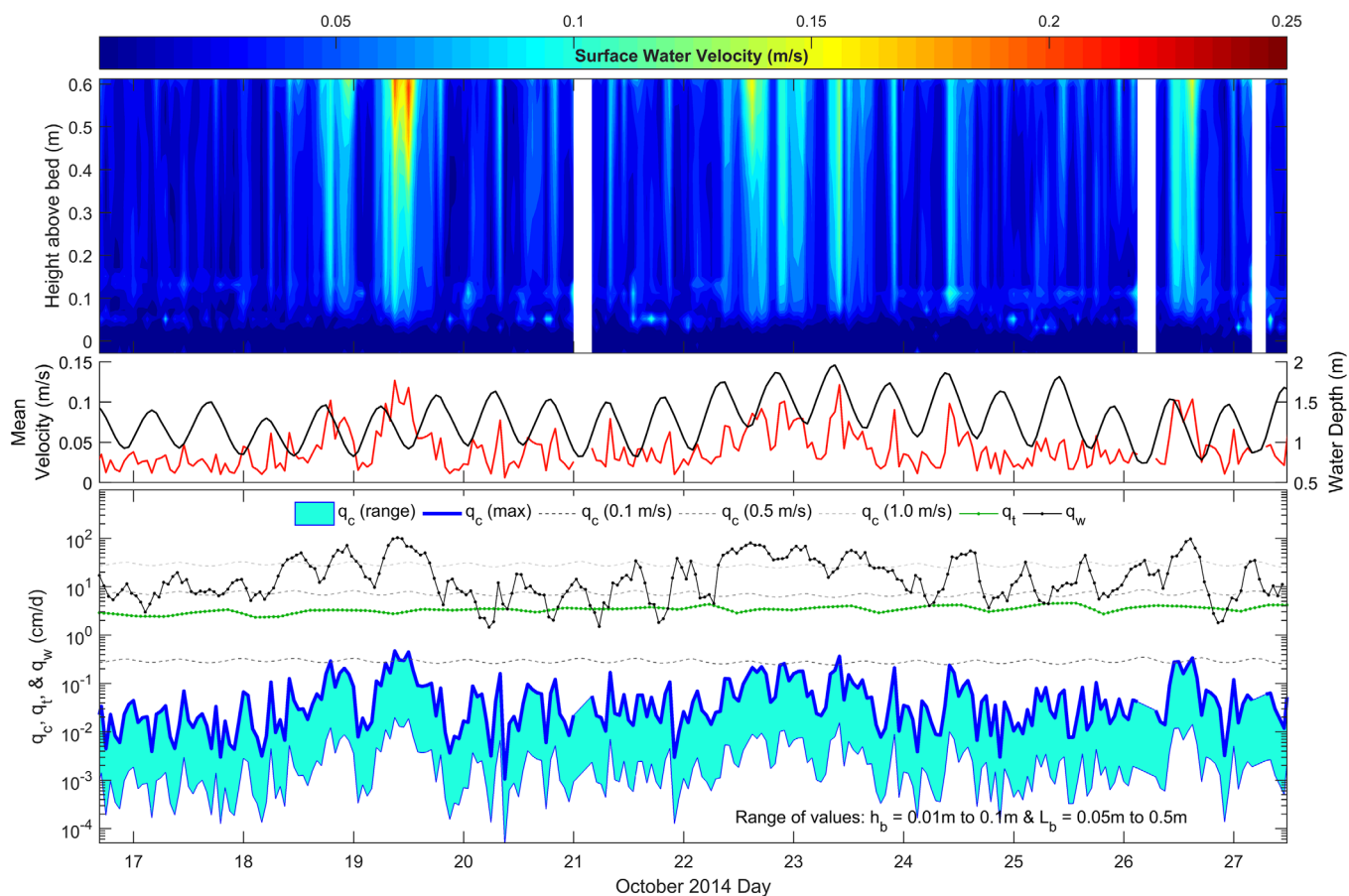


Figure 7. Current- and tide-induced benthic exchange values and the data used to calculate them. (a) Color plot of burst-averaged water column velocity profiles from down-looking ADCP. (b) Average velocity in middle third of profile (red line), and water depth (black line). (c) Wave-induced q_w (from differential pressure measurements), current-induced q_c (from measured currents and range of bed form dimensions), and tide-induced q_t (from pressure measurements).

and water depth averaged $1.28 \pm 0.27\text{ m}$ (black line in Figure 7b). Current-induced benthic exchange rates were calculated for a range of bed form dimensions ($h_b = 1\text{--}10\text{ cm}$ and $L_b = 5\text{--}50\text{ cm}$) for each burst (shaded cyan region in Figure 7c). The steepest bed forms resulted in the highest current-induced benthic exchange rates, which averaged $6.5 \times 10^{-2}\text{ cm/d}$ over the study period (thick upper blue line in Figure 7b). This exchange rate is just 0.33% of the average wave-induced exchange rate calculated from differential pressure measurements.

Tide-induced benthic exchange calculated analytically (3.70 cm/d average) was always greater than current-induced benthic exchange, but exceeded wave-induced benthic exchange in only 9 of 260 bursts (3.6%; Figure 7c, Table 1). The mean measured tidal amplitude was $0.33 \pm 0.05\text{ m}$ (range = 0.23–0.44 m) and the mean tidal period during the deployment was 12.4 h (Figure 7b). This is consistent with the finding of Sawyer et al. (2013) for simulations over the entire Delaware Inland Bays.

5. Discussion

5.1. Comparison of Wave-Induced Benthic Exchange Methods

The wave-induced benthic exchange rates obtained from differential pressure measurements and ADCP-based calculations had similar magnitudes and were well correlated ($R^2 = 0.868$; Figures 5 and 8a), which supports the validity of both methods. This goodness of fit between ADCP and differential pressure-based exchange rates was not correlated to T_w , h_w , wind direction or speed, tidal stage, or mean current velocity. The agreement between the ADCP-based method and the high-D set of groundwater flow models also supports the use of the analytical model of equation (1) to calculate exchange from wave parameters for

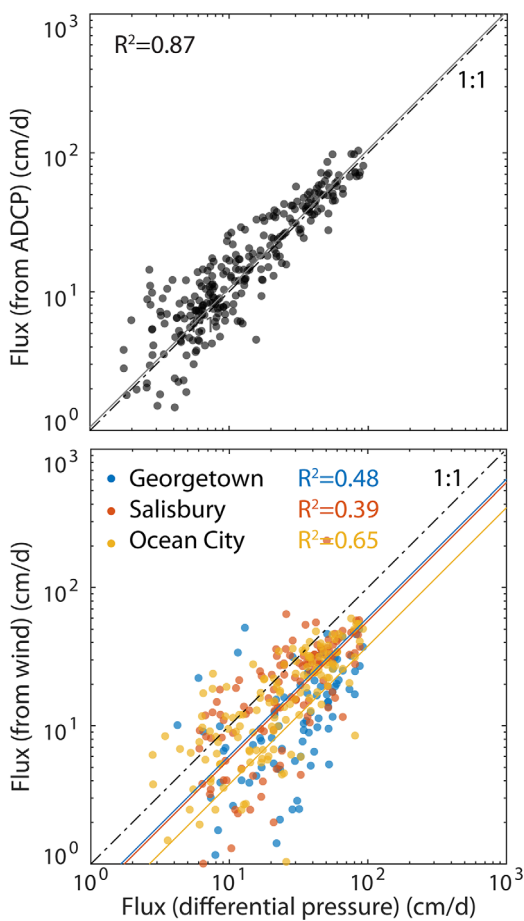


Figure 8. Comparison of benthic exchange calculation methods. (a) Differential pressure versus ADCP-measured wave parameters. (b) Differential pressure versus wind-derived wave parameters. Although plots are in log-log space for clarity, R² values in both plots are for linear, not log, comparisons.

results would require either more accurate wind data and application only at locations with greater fetch, or more complex wave models.

5.2. Exchange Zone Thickness

An empirical formula to relate D, L_w, and d_{ex} was developed by comparing d_{ex} and L_w in the eight model sets. In each of these eight model sets, a line with a zero Y-intercept was fit to d_{ex} versus L_w (supporting information Figure A3). An empirical relationship was established by plotting these eight slopes versus the D for each model set:

$$\frac{d_{ex}}{L_w} = \begin{cases} 0.188 \log_{10} D + .369, & D < 4 \\ 0.481, & D \geq 4 \end{cases} \quad (9)$$

Thus, the exchange zone depth in high-K, low-D aquifers approaches the commonly cited theoretical exchange zone thickness of $\frac{1}{2} L_w$ (e.g., King et al., 2009). However, that rough estimate greatly overestimates d_{ex} in compressible, low-K, aquifers. Seabed sediment type varies widely, but an estimate of exchange depth for reasonable sand K and S_s values gives perspective. Assuming K values for clean sand range from 10^{-6} to 10^{-3} m/s (e.g., Fetter, 2001) and S_s for sand is $\sim 10^{-3}$ m⁻¹ (supporting information Figure A1), the corresponding exchange depths range from nearly zero to the theoretical maximum ($\frac{1}{2} L_w$).

Exchange depths for current-induced flow are on the order of one bed form wavelength (Cardenas & Wilson, 2006; Elliott & Brooks, 1997; Thibodeaux & Boyle, 1987), which are assumed in this study to be less than 0.5 m (and probably much less). Tide-induced exchange depths in this estuary have been calculated to

relatively incompressible seabed sediments. A lack of agreement between these methods and the low-D numerical model suggests that sediment compressibility is an important control on wave-induced exchange in seabed aquifers composed of finer and more compressible sediments, and that the analytical model should not be used where that is the case.

ADCP-derived exchange rates frequently exceeded differential pressure-derived exchange rates and averaged 12.6% larger than the average from all five sensors (Figure 5g, Tables 1, and 2). This is likely because we are underrepresenting the real flux by including the deep pressure sensor data in these calculations. A more accurate method might be to average only shallow-sensor-based exchange rates because they capture near-seabed pressure gradients that have not attenuated with depth as much as the signal recorded by the deep pressure sensors—fluxes from the shallow sensors exceeded ADCP-derived rates by 30% (Figures 5a, 5g, and Table 1). We might expect this difference because aquifer compressibility is ignored by the ADCP method but inherent in the pressure-based method, and compression increases wave-induced benthic exchange rates across the seabed.

Wind-derived wave-induced benthic exchange rates were lower than those calculated from the ADCP (52.1%) and pressure (58.7%) data, particularly when fetch was limited (Figure 5g and Table 2). At those times, the empirical wind-generated wave model underestimated wave intensity because effects of wave spreading, hysteresis, and non-wind wave sources were unaccounted for (e.g., Herbers et al., 1999; Young & Verhagen, 1996). Prescribing a minimum T_w value, a technique employed in other wave models (e.g., Tolman, 2009) and consistent with measured wave data (Figure 5b), could improve matching. Wind data and resulting wave-induced benthic exchange rates were inconsistent among the three weather stations (Figures 5 and 8b), which illustrates the difficulty of characterizing wind over the distances between the study site and weather stations (23–43 km; Figure 1a). This method has great potential because of its ease, but improved

be on the order of millimeters to centimeters, and depend on tidal period, tidal amplitude, c , K , and effective porosity, which influence penetration and tide-induced benthic exchange (Sawyer et al., 2013). Thus, the exchange zone generated by wave-induced exchange is consistently larger (and generally much larger) than that generated by tides or currents at the Holts Landing study site.

Exchange zone thickness is likely variable on small spatial scales due to sediment heterogeneity. This can be seen by comparing the pressure data at the two sensor locations that had measurements at two depths. Pressure attenuated more rapidly with depth at Sensor 1 than at the Sensor 2 location, despite being just 1 m apart. The time-averaged absolute pressure difference at 1d was 129% of that measured at 1s, whereas the value at 2d was 185% of the 2s value. The MODFLOW model results show that this difference can be accounted for by variability in K or S_s .

5.3. Sources of Uncertainty

There are a number of uncertainties in the calculations used to estimate benthic exchange in this study. First, it is unclear how nonlinear interactions between these three mechanisms affect the resulting rates of benthic exchange (e.g., King 2012; Sawyer et al., 2013). For instance, net discharge or recharge from tides or terrestrially derived fresh discharge could impede or enhance shallow exchange mechanisms like wave- or current-induced exchange (e.g., Cardenas & Wilson, 2007). The effects of these interactions are difficult to quantify and are in need of further investigation.

Changes in seabed elevation also affect benthic exchange calculations that include water depth as a parameter. These changes can occur quickly, depending on the hydrologic and sedimentological conditions. During the deployment, reductions in seabed elevation of up to 0.5 cm were observed. This was assumed to be the result of scour lowering the seabed rather than movement of the well-anchored orifice. This seabed movement could affect the water depth used in the calculations (e.g., equations (1)–(5)). It also suggests that the sensor tube and mounting rod could impose an observer effect that affected exchange. Last, changes in orifice depth could cause variability in the assumed constant d/l term of Darcy's law and affect differential-pressure derived fluxes. The <0.5 cm bed movement could have an impact of up to 12% on the resulting wave-induced fluxes, which might explain some of the discrepancy between ADCP and differential-pressure-based exchange rates.

Error inherent to measurements made with pressure sensors also reduces the certainty of pressure-based calculations of wave-induced flux. For the K value measured in this study, the 1.4 mm error associated with each pressure sensor translates to an instantaneous exchange error of 96 cm/d for shallow sensors and 27 cm/d for deep sensors. Although some wave-induced exchange rates are within the measurement error, those rates were determined from instantaneous exchange values that well-exceed that error, so we have confidence in our calculated exchange rates. Furthermore, by subtracting the moving average during processing we removed any bias component of the error. Finally, wave-induced benthic exchange rates obtained from differential pressure measurements and ADCP-derived values correlated well even at low values (Figure 8a).

5.4. Comparisons to Larger-Scale Drivers of Exchange

The measured wave-induced benthic exchange values are similar in magnitude to flux measurements on longer temporal scales at this site. Russiello et al. (2013) and Sawyer et al. (2014) used seepage meters to characterize submarine groundwater discharge (SGD) near the location of the tripod used in this study. SGD in the area near the tripod was composed of recirculated baywater and had net discharge values ranging from 0 to 50 cm/d, which is similar in magnitude to wave-induced benthic exchange rates measured in this study. These seepage meter measurements integrated SGD at 2 h intervals, so they are characterizing a different driving mechanisms than the short-timescale associated with wave-induced exchange. Nearer to shore, these studies identified fresh SGD rates as high as 32 cm/d, so wave induced exchange rates exceed the highest measured terrestrially driven SGD.

5.5. Implications for Biogeochemical Reactions

Biotic and abiotic reaction rates in the benthic exchange zone depend on the supply of reactive solutes and the residence time of those solutes in the benthic reaction zone. Our analysis shows that surface waves have a strong control on solute fluxes, the size of the reactive zone, and the residence time in that zone, and those controls are greater than those imposed by tides and currents at our field site, a typical shallow

estuary. Thus waves strongly influence benthic reactivity and corresponding chemical fluxes through and discharging from the seabed (e.g., Cardenas et al., 2008; Shum, 1993) and influencing elemental cycling. The new understanding of spatial and temporal variability of wave-induced exchange derived from this analysis can help identify the “hot spots” and “hot moments” in submerged sediments and coastal aquifers (Briggs et al., 2014a, 2014b; Heiss et al., 2017; Marzadri et al., 2012; Zarnetske & Haggerty, 2011). In the benthic exchange zones, reactions in hot spots and during hot moments are highest when the residence timescale is similar to the reaction timescale (Gomez-Velez et al., 2015; Harvey et al., 2013). “Hot moments” of high reactivity should occur when long L_w values drive deep exchange and large h_w values generate rapid benthic exchange rates with short residence times (equations (1) and (9)). “Hot spots” should occur where high-diffusivity sediments (high K to S_s ratio) result in relatively deep mixing zone and relatively short residence times.

6. Conclusions

Benthic exchange in a shallow, sandy, microtidal estuary were quantified using six independent techniques involving field measurements, numerical simulations, and analytical models to (1) compare estimation methods, (2) characterize primary controls on the spatial and temporal variability in exchange rates, depths, and residence times, and (3) compare the relative influence of waves, tides, and currents. The agreement between wave-induced benthic exchange calculated from high-resolution differential pressure measurements across the seabed and an analytical solution based on ADCP-measured wave parameters showed that such exchange can be accurately measured with pressure sensors in field settings. Numerical ground-water model results showed that the simple analytical solution applied represents exchange well for incompressible seabed sediments but overestimates the exchange in compressible sediments. The models also showed that the depth of benthic exchange in typical seabed sediments ranged from nearly zero in more compressible sediments to a maximum depth of one-half the surface wavelength in rigid aquifers. The results can be used to predict factors that affect the biogeochemistry of benthic exchange zones and their effects on shallow estuaries where wave-induced benthic exchange is a dominant mechanism. The insights gained may aid coastal managers in quantifying nutrient and contaminant loads to and processing within estuarine and nearshore ecosystems.

Acknowledgments

The authors thank Jack Puleo, James Kirby, and Arthur Trembanis for lending field equipment, Mahfuz Khan, Carter Duval, and Margaret MacGibeny for assistance deploying and retrieving equipment, Caitlyn Sarno for assistance with sediment analysis, Audrey Sawyer for constructive comments on experimental design, Leonard Konikow for modeling assistance, and Adam Skarke and Ryan Mieras for assistance processing field data. The paper benefitted from the feedback of Jud Harvey and an anonymous reviewer. This work was funded by the National Science Foundation EAR-0910756 and EAR-1246554 and the University of Delaware Office of Graduate and Professional Education Summer Doctoral Fellowship. Data may be accessed from the CUAHSI HydroShare database (Russoniello et al., 2017).

References

- Andres, A. S., Michael, H., Russoniello, C. J., Fernandez, C., He, C., & Madsen, J. A. (2017). *Investigation of submarine groundwater discharge at Holts Landing State Park, Delaware: Hydrogeologic framework, groundwater level and salinity observations* (Rep. Invest. 80). Newark, DE: Delaware Geological Survey, University of Delaware.
- Berg, P., Glud, R. N., Hume, A. C., Stahl, H., Oguri, K., Meyer, V., et al. (2009). Eddy correlation measurements of oxygen uptake in deep ocean sediments. *Limnology and Oceanography Methods*, 7, 576–584. <https://doi.org/10.4319/lom.2009.7.576>.
- Boano, F., Harvey, J. W., Marion, A., Packman, A. I., Revelli, R., Ridolfi, L., et al. (2014). Hyporheic flow and transport processes: Mechanisms, models, and biogeochemical implications. *Reviews of Geophysics*, 52, 603–679. <https://doi.org/10.1002/2012RG000417>
- Bratton, J. F., Böhlke, J. K., Manheim, F. T., & Krantz, D. E. (2004). Ground water beneath coastal bays of the Delmarva Peninsula: Ages and nutrients. *Ground Water*, 42(7), 1021–1034. <https://doi.org/10.1111/j.1745-6584.2004.tb02641.x>
- Briggs, M. A., Lautz, L. K., Buckley, S. F., & Lane, J. W. (2014a). Practical limitations on the use of diurnal temperature signals to quantify groundwater upwelling. *Journal of Hydrology*, 519(Part B), 1739–1751. <https://doi.org/10.1016/j.jhydrol.2014.09.030>
- Briggs, M. A., Lautz, L. K., & Hare, D. K. (2014b). Residence time control on hot moments of net nitrate production and uptake in the hyporheic zone. *Hydrological Processes*, 28(11), 3741–3751. <https://doi.org/10.1002/hyp.9921>
- Briggs, M. A., Lautz, L. K., McKenzie, J. M., Gordon, R. P., & Hare, D. K. (2012). Using high-resolution distributed temperature sensing to quantify spatial and temporal variability in vertical hyporheic flux. *Water Resources Research*, 48(2), W02527. <https://doi.org/10.1029/2011WR011227>
- Cardenas, M. B., Cook, P. L. M., Jiang, H., & Traykovski, P. (2008). Constraining denitrification in permeable wave-influenced marine sediments using linked hydrodynamic and biogeochemical modeling. *Earth and Planetary Science Letters*, 275(1–2), 127–137. <https://doi.org/10.1016/j.epsl.2008.08.016>
- Cardenas, M. B., & Wilson, J. (2006). The influence of ambient groundwater discharge on exchange zones induced by current–bedform interactions. *Journal of Hydrology*, 331, 103–109. <https://doi.org/10.1016/j.jhydrol.2006.05.012>
- Cardenas, M. B., & Wilson, J. (2007). Exchange across a sediment–water interface with ambient groundwater discharge. *Advances in Water Resources*, 30, 301–313. <https://doi.org/10.1016/j.advwatres.2006.06.009>
- Crusius, J., Berg, P., Koopmans, D. J., & Erban, L. (2008). Eddy correlation measurements of submarine groundwater discharge. *Marine Chemistry*, 109(1–2), 77–85. <https://doi.org/10.1016/j.marchem.2007.12.004>
- Devlin, J. F. (2015). HydroGeoSieveXL: An Excel-based tool to estimate hydraulic conductivity from grain-size analysis. *Hydrogeology Journal*, 23(4), 837–844. <https://doi.org/10.1007/s10040-015-1255-0>
- Elliott, A. H., & Brooks, N. H. (1997). Transfer of nonsorbing solutes to a streambed with bed forms: Theory. *Water Resources Research*, 33(1), 123–136.
- Fehlman, H. M. (1985). *Resistance components and velocity distributions of open channel flows over bedforms (M.S. thesis)*. Fort Collins: Colorado State University.

- Ferris, J. G. (1952). *Cyclic fluctuations of water level as a basis for determining aquifer transmissibility* (U.S. Geol. Surv. Ground Water Rep. 1, 16 p.). Washington, DC: U.S. Geological Survey.
- Fetter, C. W. (2001). *Applied hydrogeology* (4th ed.). Upper Saddle River, NJ: Prentice Hall.
- Gomez-Velez, J. D., Harvey, J. W., Cardenas, M. B., & Kiel, B. (2015). Denitrification in the Mississippi river network controlled by flow through river bedforms. *Nature Geoscience*, 8, 941–945. <https://doi.org/10.1038/ngeo2567>
- Harbaugh, A. W., Banta, E. R., Hill, M. C., & McDonald, M. G. (2000). *MODFLOW-2000, the U.S. Geological Survey modular ground-water model—user guide to modularization concepts and the ground-water flow process* (U.S. Geol. Surv. Open File Rep. 00-92, 121 p.). Reston, VA: U.S. Geological Survey.
- Harrison, W., Musgrave, D., & Resburgh, W. (1983). A wave-induced transport process in marine sediments. *Journal of Geophysical Research*, 88(C12), 7617–7622. <https://doi.org/10.1029/JC088iC12p07617>
- Harvey, J. W., Böhlke, J. K., Voytek, M. A., Scott, D., & Tobias, C. R. (2013). Hyporheic zone denitrification: Controls on effective reaction depth and contribution to whole-stream mass balance. *Water Resources Research*, 49, 6298–6316. <https://doi.org/10.1002/wrcr.20492>
- Heiss, J. W., Post, V. E. A., Laattee, T., Russiello, C. J., & Michael, H. A. (2017). Physical controls on biogeochemical processes in intertidal zones of beach aquifers. *Water Resources Research*, 53, 9225–9244. <https://doi.org/10.1002/2017WR021110>
- Herbers, T. H. C., Elgar, S., & Guza, R. T. (1999). Directional spreading of waves in the nearshore zone. *Journal of Geophysical Research*, 104(C4), 7683–7693. <https://doi.org/10.1029/1998JC000092>
- Huettel, M., Berg, P., & Kostka, J. E. (2014). Benthic exchange and biogeochemical cycling in permeable sediments. *Annual Review of Marine Science*, 6, 23–51. <https://doi.org/10.1146/annurev-marine-051413-012706>
- Jeng, D. S., Barry, D. A., & Li, L. (2001). Water wave-driven seepage in marine sediments. *Advances in Water Resources*, 24(1), 1–10. [https://doi.org/10.1016/S0309-1708\(00\)00036-1](https://doi.org/10.1016/S0309-1708(00)00036-1)
- King, J. N. (2012). Synthesis of benthic flux components in the Patos Lagoon coastal zone, Rio Grande do Sul, Brazil. *Water Resources Research*, 48, W12530. <https://doi.org/10.1029/2011WR011477>
- King, J. N., Mehta, A. J., & Dean, R. G. (2009). Generalized analytical model for benthic water flux forced by surface gravity waves. *Journal of Geophysical Research*, 114, C04004. <https://doi.org/10.1029/2008JC005116>
- Latham, W., & Lewis, K. (2012). *The Contribution of the Coastal Economy to the State of Delaware*. Newark, DE: Delaware Sea Grant.
- Marzadri, A., Tonina, D., & Bellin, A. (2012). Morphodynamic controls on redox conditions and on nitrogen dynamics within the hyporheic zone: Application to gravel bed rivers with alternate-bar morphology. *Journal of Geophysical Research*, 117, G00N10. <https://doi.org/10.1029/2012JG001966>
- Merritt, M. L. (2004). *Estimating Hydraulic Properties of the Floridian Aquifer System by Analysis of Effects. Collier and Hendry Counties, Florida* (U.S. Geol. Surv. Water-Resour. Invest. Rep. 03-4267, 70 p.). Reston, VA: U.S. Geological Survey.
- Michael, H. A., Charette, M. A., & Harvey, C. F. (2011). Patterns and variability of groundwater flow and radium activity at the coast: A case study from Waquoit Bay, Massachusetts. *Marine Chemistry*, 127(1–4), 100–114. <https://doi.org/10.1016/j.marchem.2011.08.001>
- Michael, H. A., Lubetsky, J., & Harvey, C. (2003). Characterizing submarine groundwater discharge: A seepage meter study in Waquoit Bay, Massachusetts. *Geophysical Research Letters*, 30(6), 1297. <https://doi.org/10.1029/2002GL016000>
- Mu, Y., Cheng, A. H.-D., Badiey, M., & Bennett, R. (1999). Water wave driven seepage in sediment and parameter inversion based on pore pressure data. *International Journal for Numerical and Analytical Methods in Geomechanics*, 23(13), 1655–1674. [https://doi.org/10.1002/\(SICI\)1096-9853\(199911\)23:13<1655::AID-NAG61>3.0.CO;2-D](https://doi.org/10.1002/(SICI)1096-9853(199911)23:13<1655::AID-NAG61>3.0.CO;2-D)
- National Climatic Data Center (NCDC). (2016). *Quality controlled local climatological data ASCII Files*. Asheville, NC: National Climatic Data Center. Retrieved from <https://www.ncdc.noaa.gov/orders/qlcld/>
- Nelson, J. R., Eckman, J. E., Robertson, C. Y., Marinelli, R. L., & Jahnke, R. A. (1999). Benthic microalgal biomass and irradiance at the sea floor on the continental shelf of the South Atlantic Bight: Spatial and temporal variability and storm effects. *Continental Shelf Research*, 19(4), 477–505. [https://doi.org/10.1016/S0278-4343\(98\)00092-2](https://doi.org/10.1016/S0278-4343(98)00092-2)
- Nortek-AS. (2015). *Aquadopp HR-Profiler Factsheet*. Oslo, Norway: Nortek AS.
- Reid, R. O., & Kajiura, K. (1957). On the damping of gravity waves over a permeable sea bed. *Transactions of the American Geophysical Union*, 38(5), 662–666. <https://doi.org/10.1029/TR038i005p00662>
- Riedl, R. J., Huang, N., & Machan, R. (1972). The subtidal pump: a mechanism of interstitial water exchange by wave action. *Marine Biology*, 13(3), 210–221. <https://doi.org/10.1007/BF00391379>
- Rosenberry, D. O. (2008). A seepage meter designed for use in flowing water. *Journal of Hydrology*, 359(1–2), 118–130. <https://doi.org/10.1016/j.jhydrol.2008.06.029>
- Rosenberry, D. O., & Morin, R. H. (2004). Use of an electromagnetic seepage meter to investigate temporal variability in lake seepage. *Ground Water*, 42, 68–77. <https://doi.org/10.1111/j.1745-6584.2004.tb02451.x>
- Russoniello, C., Heiss, J., & Michael, H. (2017). *Variability in benthic exchange rate, depth, and residence time beneath a shallow coastal estuary*. HydroShare. Retrieved from <http://www.hydroshare.org/resource/d1c980ba6dd741db6931b8758f3abe2>
- Russoniello, C. J., Fernandez, C., Brattton, J. F., Banaszak, J. F., Krantz, D. E., Andres, A. S., et al. (2013). Geologic effects on groundwater salinity and discharge into an estuary. *Journal of Hydrology*, 498, 1–12. <https://doi.org/10.1016/j.jhydrol.2013.05.049>
- Russoniello, C. J., & Michael, H. A. (2015). Investigation of seepage meter measurements in steady flow and wave conditions. *Groundwater*, 53(6), 959–966. <https://doi.org/10.1111/gwat.12302>
- Santos, I. R., Eyre, B. D., & Huettel, M. (2012). The driving forces of porewater and groundwater flow in permeable coastal sediments: A review. *Estuarine, Coastal and Shelf Science*, 98, 1–15. <https://doi.org/10.1016/j.ecss.2011.10.024>
- Sawyer, A. H. (2015). Enhanced removal of groundwater-borne nitrate in heterogeneous aquatic sediments. *Geophysical Research Letters*, 42, 403–410. <https://doi.org/10.1002/2014GL062234>
- Sawyer, A. H., Cardenas, M. B., & Buttles, J. (2011). Hyporheic exchange due to channel-spanning logs. *Water Resources Research*, 47, W08502. <https://doi.org/10.1029/2011WR010484>
- Sawyer, A. H., Lazareva, O., Kroeger, K. D., Crespo, K., Chan, C. S., Stiegitz, T., et al. (2014). Stratigraphic controls on fluid and solute fluxes across the sediment-water interface of an estuary. *Limnology and Oceanography*, 59(3), 997–1010. <https://doi.org/10.4319/lo.2014.59.3.0997>
- Sawyer, A. H., Shi, F., Kirby, J. T., & Michael, H. A. (2013). Dynamic response of surface water-groundwater exchange to currents, tides, and waves in a shallow estuary. *Journal of Geophysical Research: Oceans*, 118, 1749–1758. <https://doi.org/10.1002/jgrc.20154>
- Seitzinger, S. P., Harrison, J. A., Böhlke, J. K., Bouwman, A. F., Lowrance, R., Peterson, B., et al. (2006). Denitrification across landscapes and waterscapes: A synthesis. *Ecological Applications*, 16(6), 2064–2090. [https://doi.org/10.1890/1051-0761\(2006\)016\[2064:DALAWA\]2.0.CO;2](https://doi.org/10.1890/1051-0761(2006)016[2064:DALAWA]2.0.CO;2)
- Shum, K. T. (1993). The effects of wave-induced pore-water circulation on the transport of reactive solutes below a rippled sediment bed. *Journal of Geophysical Research*, 98(C6), 10289–10301. <https://doi.org/10.1029/93jc00787>

- Shum, K. T., & Sundby, B. (1996). Organic matter processing in continental shelf sediments—The subtidal pump revisited. *Marine Chemistry*, 53(1–2), 81–87. [https://doi.org/10.1016/0304-4203\(96\)00014-X](https://doi.org/10.1016/0304-4203(96)00014-X)
- Smith, A. J., Herne, D. E., & Turner, J. V. (2009). Wave effects on submarine groundwater seepage measurement. *Advances in Water Resources*, 32(6), 820–833. <https://doi.org/10.1016/j.advwatres.2009.02.003>
- Thibodeaux, L. J., & Boyle, J. D. (1987). Bedform-generated convective transport in bottom sediment. *Nature*, 325, 341–343. <https://doi.org/10.1038/325341a0>
- Tolman, H. L. (2009). *User manual and system documentation of WAVEWATCH-IIITM version 3.14* (Environmental Modeling Center Tech. Note 276). Camp Springs, MD: NOAA NWS National Centers for Environmental Prediction.
- Validyne. (2014). *P24 datasheet*. Northridge, CA: Validyne Engineering.
- Walch, M., Seldomridge, E., Mcgowan, A., Boswell, S., & Bason, C. (2016). *2016 State of the inland bays*. Rehoboth Beach, DE: Center for the Inland Bays.
- Wang, H. F. (2000). *Theory of linear poroelasticity with applications to geomechanics and hydrogeology* (p. 287). Princeton, NJ: Princeton University Press.
- Wilson, A. M., Woodward, G. L., & Savidge, W. B. (2016). Using heat as a tracer to estimate the depth of rapid porewater advection below the sediment-water interface. *Journal of Hydrology*, 538, 743–753. <https://doi.org/10.1016/j.jhydrol.2016.04.047>
- Yamamoto, T., Koning, H. L., Sellmeijer, H., & Van Huijum, E. (1978). On the response of a poro-elastic bed to water waves. *Journal of Fluid Mechanics*, 87, 193–206. <https://doi.org/10.1017/S0022112078003006>
- Young, I. R., & Verhagen, L. A. (1996). The growth of fetch limited waves in water of finite depth. Part 1. Total energy and peak frequency. *Coastal Engineering*, 29(1–2), 47–78. [https://doi.org/10.1016/S0378-3839\(96\)00006-3](https://doi.org/10.1016/S0378-3839(96)00006-3)
- Younger, P. L. (1993). Simple generalized methods for estimating aquifer storage parameters. *Quarterly Journal of Engineering Geology and Hydrogeology*, 26(2), 127–135. <https://doi.org/10.1144/GSL.QJEG.1993.026.02.04>
- Zarnetske, J., & Haggerty, R. (2011). Dynamics of nitrate production and removal as a function of residence time in the hyporheic zone. *Journal of Geophysical Research*, 116, G01025. <https://doi.org/10.1029/2010JG001356>
- Ziebis, W., Huettel, M., & Forster, S. (1996). Impact of biogenic sediment topography on oxygen fluxes in permeable seabeds. *Marine Ecology Progress Series*, 140, 227–237. <https://doi.org/10.3354/meps240227>